ACTUATION OF AN ADAPTIVE SHOCK CONTROL BUMP USING PRESSURIZED CHAMBERS

Nuno Alves de Sousa, NAS[*] Afzal Suleman, AS[*†] Markus Kintscher, MK[‡]

[*]*Instituto Superior Técnico, Universidade de Lisboa*
Av. Rovisco Pais, 1, 1049-001 Lisboa, Portugal

[†]*Professor and Canada Research Chair, University of Victoria, Canada*

[‡] *Deutsches Zentrum für Luft- und Raumfahrt*
Institut für Faserverbundleichtbau und Adaptronik, Braunschweig, Deutschland

E-mail of the corresponding author: nunoalvesdesousa@me.com

ABSTRACT

The dawn of research on shock and boundary layer interaction control dates back to the 1970's, when humped transonic aerofoils were first studied as a means to improve the performance of supercritical aerofoil technology at off-design conditions. Since then, shock control bumps (SCBs) have been found to be promising devices for such kind of flow control. They have a smearing effect on the shock wave structure achieved through isentropic pre-compression of the flow upstream of the main shock and can significantly lower wave drag without incurring unacceptable viscous losses. However, their performance is strongly dependent on a set of geometrical parameters which must be adjusted according to the ever-changing flight conditions.

A concept for an adaptive SCB is therefore presented. The proposed actuation mechanism aims at a compact, lightweight and simple structure which could be integrated in the spoiler region of near-future aircraft without major design changes required. Numerical optimization of a simplified analytical model of the structure is used to investigate the SCB adaptation to various aerodynamic target shapes. Compromises between geometrical conformity and both structural and actuation related requirements are studied. Furthermore, an outlook is given on design issues related to three-dimensional effects on a finite-width SCB.

KEYWORDS: Shock control bump; wave drag minimization; morphing spoiler; pressure actuated adaptive structure; structural optimization.

1. INTRODUCTION

Aircraft manufacturers are aware that even small efficiency gains can represent substantial savings for air operators in the ever more competitive air transport sector. Therefore, modern aircraft technologies are focusing on the reduction of DOCs and increase in mission flexibility as a means to achieve a competitive advantage. Most of high economic and industrial impact technologies are dependent on the optimization of the aerodynamic efficiency of the main wing which has long been an area of design compromises for the engineer: a narrower cruise envelope leads to higher efficiency gains with worse off-design performance, while a wider cruise envelope means less efficiency gains within the operating conditions.

Large scale morphing technologies dealing with the adaptation of the entire wing as described by Smith et al. [1] ensure that each operating point is a design optimum. Nevertheless, this approach requires complex actuation mechanisms and can be seen as a long-term solution. A more feasible approach would be adapting the aerofoil geometry by focusing on individual movables *i.e.* leading edge, flaps and spoilers. In fact, the EUROSHOCK I & II programs [2, 3] showed that the use of a bump in order to adapt a relatively small portion of the suction side of the main wing as initially proposed by Ashill et al. [4] is an effective way of minimizing wave drag due to the strong shock waves that develop at transonic cruise conditions. Thereafter, the so-called shock control bump (SCB) has been subject to various aerodynamic investigations and its role as a flow control device is becoming increasingly popular.

This study focuses on the structural realization and actuation of such devices. It is therefore useful to first introduce basic aerodynamic principles regarding SCBs in order to understand how they relate to structural constraints.

2. AERODYNAMIC PRINCIPLES

Increasing the free-stream Mach number (M_∞) or angle of incidence (lift) of a transonic aerofoil will lead to the development of a supersonic region on the upper surface. For a modern turbulent design, the supersonic flow will usually be terminated by an isentropic recompression or a weak shock wave as shown in figure 1 (T). If either free-stream parameter is increased, commonly the shock will strengthen leading to extra wave drag culminating in separation which defines the drag-rise and buffet boundaries. For a laminar aerofoil - figure 1 (L) - the flow undergoes a continuous acceleration on the upper surface causing stronger shock waves even for the design conditions.

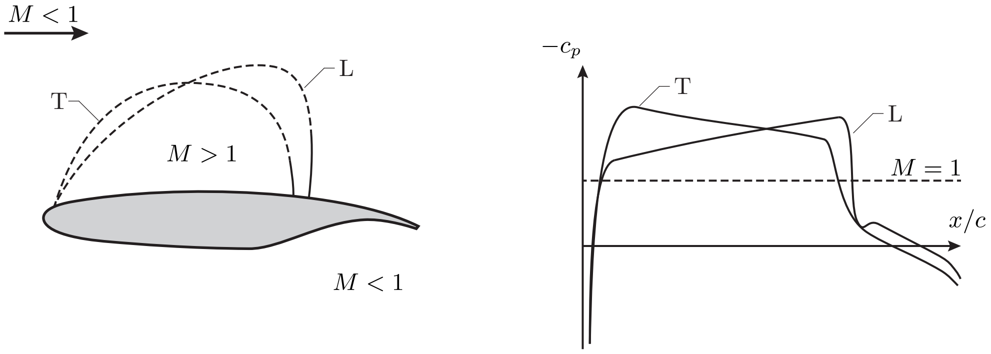

(a) Shock configuration (b) Pressure distribution

Figure 1 – Transonic flow for a turbulent (T) and a laminar (L) aerofoil at equal lift.

Across the shock entropy increases and total pressure decreases. Wave drag is then generated and it seriously limits cruise efficiency of current aircraft configurations.

SCBs can split the stronger single shock into a series of weaker oblique shocks or compression waves that decelerate the flow more isentropically, *i.e.* gradually, than the uncontrolled shock wave. The result is a reduced stagnation pressure loss across the shock leading to lower drag. Figure 2 illustrates the principle of operation of SCBs in transonic flight.

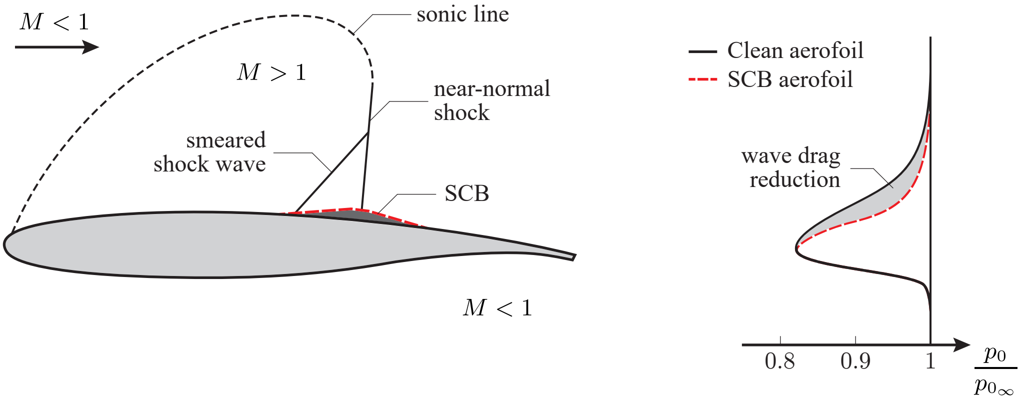

(a) Transonic flow structure showing the λ-shock foot structure (b) Total pressure in the wake

Figure 2 – Illustration of the principle of operation of a SCB on a supercritical wing.

SCB geometry is usually comprised of a ramp upstream of the nominal shock position, a short crest region and a tail. The function of the ramp is to generate an oblique shock or multiple oblique compression waves ahead of the main shock deflecting the incoming supersonic flow away from the surface. Close to the crest, a near-normal shock decelerates the flow to subsonic velocities. The tail then brings the post-shock flow back to the aerofoil surface.

SCBs can be classified as two or three-dimensional: two-dimensional (2D) SCBs have a constant profile along the wing span; three-dimensional (3D) SCBs correspond to a series of finite-width bumps distributed along the wing. This work will focus on 2D SCBs as they present the highest potential for efficiency gains.

Figure 3 summarizes the characteristic geometric parameters of a SCB: the bump is located on an aerofoil surface of chord c at a position x_0 from the leading edge. It has a crest of length c_B and height h_B, which is schematically represented by point $C(c_B, h_B)$. The bump is also defined by its length l_B and its shape f_B.

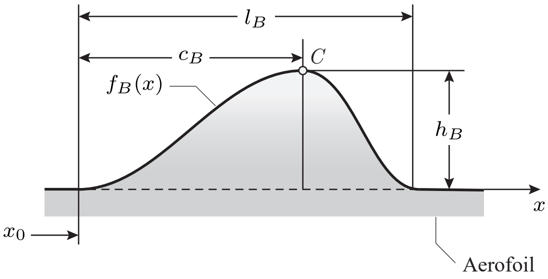

Figure 3 – Definition of characteristic geometric parameters for 2D SCBs

Symbol	Parameter	Typical values
h_B	SCB height	$\delta_0 \pm \delta_0$
l_B	SCB length	$\frac{l_B}{c} \in [12\%\,;20\%]$
c_B	Crest length	$\frac{c_B}{l_B} \in [30\%\,;80\%]$
x_S	Relative shock location[1]	$[-10\%\,;15\%]$

Table 1 – Characteristic SCB parameters and typical values investigated.

Table 1 shows reference ranges considered by a multitude of aerodynamic studies on SCBs. The most significant aspect to retain is probably the fact that SCB research has essentially focused on bumps with heights of the order of the local boundary layer thickness. Additionally, typical peak shock strength is around $M = 1.3 \pm 0.2$.

2.1. Aerodynamic Performance of SCBs

Previous works by Dargel et al. [5] and Sommerer et al. [6] have shown that the drag reduction potential of SCBs depends strongly on the correct bump position, height and location of the bump maximum. The bump height depends on the actual flight conditions and the aerofoil geometry, but can be estimated to be within 0.5 percent of the local chord length. An interesting result from these investigations is the fact that the detailed bump shape does not have a strong effect on the bump effectiveness.

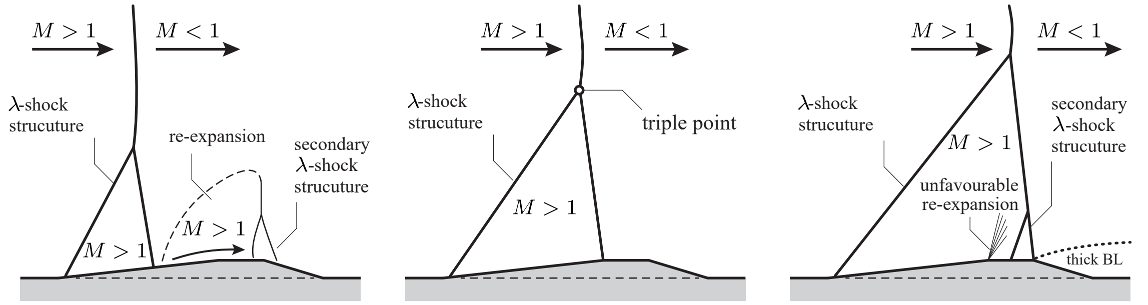

(a) Shock upstream of the optimum location

(b) Shock at the optimum location

(c) Shock downstream of the optimum location

Figure 4 – Impact of shock position on the flow structure generated by a straight ramp, straight tail SCB.

Figure 4 is helpful in understanding why the bump position, height and location of the bump maximum play a major role in SCB performance. When the shock is at the optimum location - figure 4(b) - a “cleaner presure” rise has the least negative effect on the boundary layer. The off-design cases - figures 4(a) and (c) - introduce a re-expansion and secondary shock structures which significantly impact the incoming boundary layer: when the shock is upstream of the optimum location, the bump accelerates the flow forming a secondary shock - figure 4(a); when the shock is downstream of the optimum location, there is an unfavourable expansion over the bump crest leading to a stronger shock and ultimately to boundary layer separation - figure 4(c). As a consequence, static SCBs present a narrow region of effectiveness. When the flight conditions lead to non-optimum shock locations SCB performance is worse than that of a clean aerofoil. Since there is some shock mobility during cruise, it is essential to be able to continuously adapt the significant SCB parameters according to the actual shock position. This sets the case for an adaptive SCB, where the main actuation objective is the ability to adjust the crest position.

---

[1] Relative shock location $x_S \equiv \frac{x_0 + c_B - x_{\text{shock}}}{c}$

3. STRUCTURAL CONCEPT, MODEL AND OPTIMIZATION

While there are numerous publications dealing with the aerodynamic design of SCBs, the structural realization of such a structure-system is still a key challenge. For current transport aircraft, even though during flight shock movement is always an obstacle, the shock location is generally restricted to the rear portion of the wing, *i.e.* the region closer to the spoilers and the wing trailing edge. In order to allow an easy integration of SCBs in near-future transport aircraft, the proposed system location is the spoiler region. The available design space is therefore extremely limited and the main drivers for concept selection should be: a compact design, lightweight structure and low complexity actuation mechanism for the SCB deployment.

3.1. Concept

The main design objective is to achieve a structure capable of conforming to prescribed optimal aerodynamic bump shapes (or at least a set of crest positions) while having enough structural stiffness in order to resist aerodynamic loads. Therefore, a new integral spoiler structure has been selected.

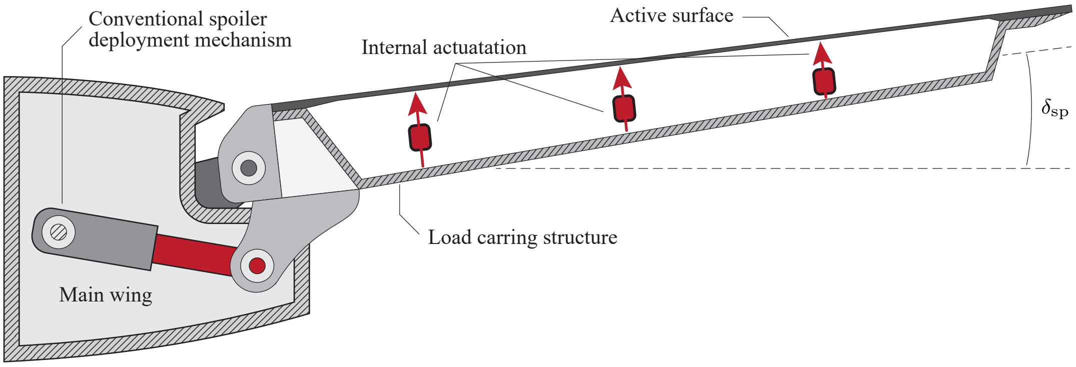

Figure 5 – The integral spoiler structure

The new integral spoiler structure is comprised of three layers: the top layer is an active surface where the SCB is generated, the bottom layer is a load-carrying structure which supports both aerodynamic loads as well as actuation loads for the SCB and the middle layer is where the internal actuation mechanism for the SCB deployment is fitted. This approach does not require a complete redesign of the spoiler deployment mechanism since the actuation of the SCB is independent of the spoiler deployment mechanism. The passive structure greatly simplifies the design of the SCB actuation system as it provides the necessary support for the actuation loads.

This design approach separates the functional (active) structure from the supporting structure thanks to a mechanical parallel actuation system as Wadehn et al. [7] and Bein et al. [8] proposed. These authors also proposed the use shape-memory alloy (SMA) actuated deformation and pressurized tube springs as variations on the linear actuator for internal actuation. However, this approach requires the use of numerous actuators.

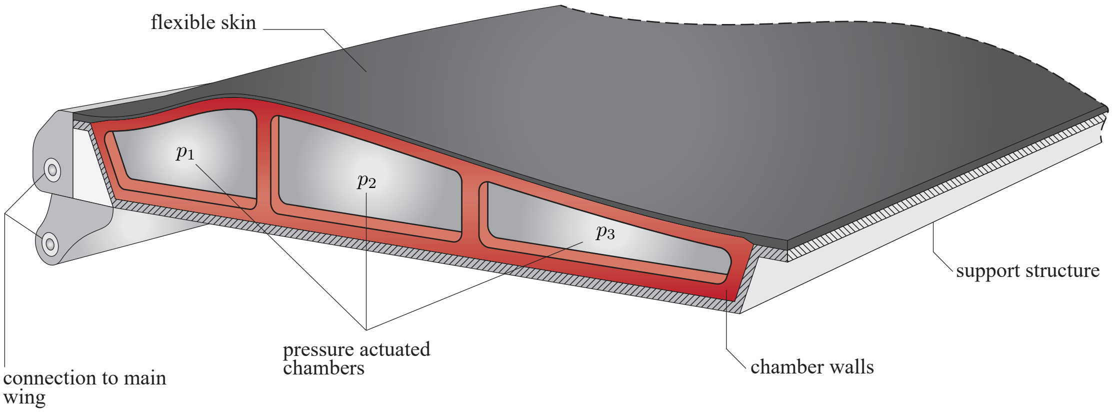

Figure 6 – Spoiler concept with pressurized chambers for an adaptive SCB

A spoiler concept using pressurized chambers was selected as a pioneering actuation technology that is able to combine the key requirements. The SCB deployment and its adaptation to the changing flight conditions is realized by differential pressurization of chambers inside the spoiler body, as shown in figure 6. A series of multiple chambers could be combined into one single part during manufacturing. This reduces the actuation mechanism to a sealed assembly that can easily be replaced in case of a repair. The chambers are supported by the conventional load-carrying structure and spanwise stiffeners can be designed according to the needs of the parallel actuation system using stringers embedded into the interfaces (chamber walls) between each chamber. Therefore, the cross-sectional stringer shape must be designed to allow deformation in the direction of the chamber height while at the same time providing spanwise support. Since pressure acts uniformly across the entire span of the spoiler, spanwise waviness issues are not expected. Moreover, the elastomeric material of the chamber walls allows for a compact and lightweight mechanism. Finally, since pressure is allowed to act on the entire portion of the flexible skin that contacts each chamber, it is predictable that the number of chambers, *i.e.* actuators, might be reduced when compared to previous concepts, also contributing to a more compact and lightweight structure.

3.2. Analytical Model

A design tool was developed to provide a systematic way of investigating key structural and functional interdependencies related to the actuation of the selected design concept. This tool aims to provide the foundations for an accurate sizing of the functional layer of the SCB and give an insight on the trade-offs between structural integrity and geometrical conformity qualities that the engineer will face. The simplified analytical model used by the design tool is now presented.

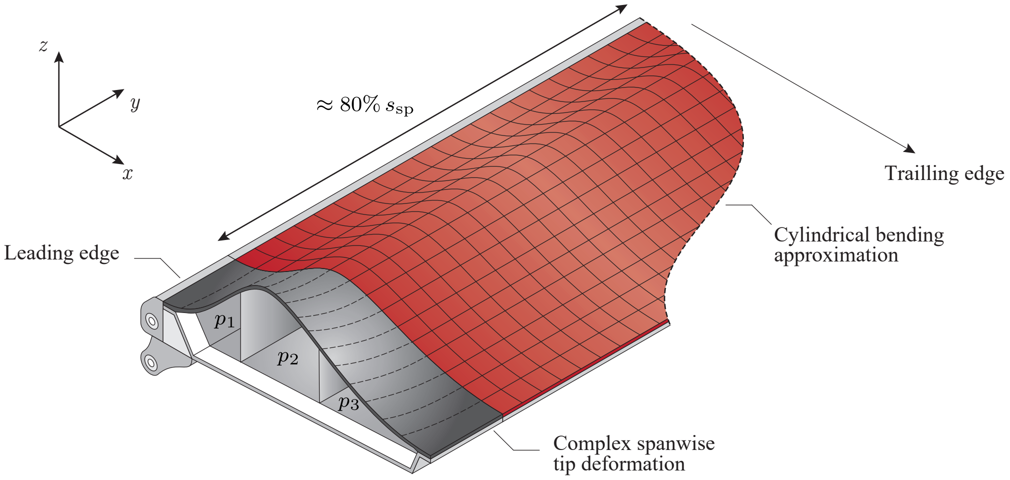

Figure 7 – Simplified structural model showing typical deformation regions of the active surface.

Figure 7 shows the simplified spoiler model where the x and y coordinate directions are the chordwise and spanwise directions, respectively. The upper spoiler skin is modelled as a transversely loaded plate while the main lower body is assumed to be comparably much stiffer. The upper skin is clamped to the support structure and free at the spoiler tips. Given that the considered SCB height to length ratios are usually bellow 1%, small strains and moderate rotations are expected. For this reason, the Kirchhoff plate theory will be used. For transversely loaded Kirchhoff plates, the static bending equation is

$$D_{11}\frac{\partial^4 w_0}{\partial x^4}+2(D_{12}+2D_{66})\frac{\partial^4 w_0}{\partial x^2\partial y^2}+D_{22}\frac{\partial^4 w_0}{\partial y^4}=q(x,y) \tag{1}$$

where w_0 is the transverse displacement of a point on the plate midplane, D_{ij} are the *bending stiffnesses* and q is the distributed transverse loading. Considering a reference frame centred at the spoiler leading edge, the boundary conditions for the clamped edges are given by

$$\Gamma_u : \quad w_0 = 0 \quad , \quad \left.\frac{\partial w_0}{\partial n}\right|_{n=x} = 0 \quad , \quad x = \{0, l_B\} \tag{2}$$

where Γ_u indicates essential boundary conditions, n is the direction normal to the clamped edge and l_b is the bump length. For the free-edges, natural boundary conditions are defined using the bending moment M_{nn} and the

Kirchhoff free-edge condition:

$$\Gamma_\sigma : \quad M_{nn} = 0 \quad , \quad V_n \equiv Q_n + \frac{\partial M_{ns}}{\partial s} = 0 \quad , \quad y = \pm\frac{s_{\text{sp}}}{2} \tag{3}$$

where V_n is the total vertical force given in terms of the vertical resultant Q_n and moment M_{ns} and s_{sp} is the spoiler span. The first index represents the normal direction to the edge surface. For the moments, the second index is the direction along which the force causing the moment is acting. Once more, n is the normal to the free-edge, *i.e.* $\hat{e}_y$ and s is the tangent direction to the free edge *i.e.*, $\hat{e}_x$.

The materials investigated will be restricted to single layer specially orthotropic and isotropic laminates. For these cases, the bending stiffnesses, vertical resultant and moments can be written in terms of the lamina engineering constants and equation 1 can be recasted into:

$$\frac{\partial^4 w_0}{\partial x^4} + 2\left[\nu_{21} + 2\frac{G_{12}}{E_1}(1-\nu_{12}\nu_{21})\right]\frac{\partial^4 w_0}{\partial x^2 \partial y^2} + \frac{\nu_{21}}{\nu_{12}}\frac{\partial^4 w_0}{\partial y^4} = \frac{q}{D^*} \quad , \quad D^* \equiv \frac{E_1 h^3}{12(1-\nu_{12}\nu_{21})} \tag{4}$$

where h is the laminate thickness. The boundary conditions, can also be written in terms of the displacement w_0. For the natural boundary conditions, laminate constitutive equations for specially orthotropic materials have been used to resolve the forces and moments in equation 3 into the displacement w_0:

$$\Gamma_u : \quad w_0 = 0 \quad , \quad \frac{\partial w_0}{\partial x} = 0 \quad , \quad x = \{0, l_B\} \tag{5a}$$

$$\Gamma_\sigma : \quad \nu_{12}\frac{\partial^2 w_0}{\partial x^2} + \frac{\partial^2 w_0}{\partial y^2} = 0 \quad , \quad \left(\nu_{12} + 4\frac{G_{12}}{E_2}(1-\nu_{12}\nu_{21})\right)\frac{\partial^3 w_0}{\partial x^2 \partial y} + \frac{\partial^3 w_0}{\partial y^3} = 0 \quad , \quad y = \pm\frac{s_{\text{sp}}}{2} \tag{5b}$$

The natural boundary conditions in equation (5b) require approximate analytical solution methods like the Ritz method or numerical methods like the FEM. However, if the SCB span to length ratio is large enough, and assuming that the pressurization of the chambers is sufficiently uniform, $y \gg x$ and $q \approx q(x)$. Under these circumstances, the central portion of the active layer behaves as a long semi-infinite plate strip and the cylindrical bending approximation greatly simplifies the solution of equation 4 by reducing the problem to one dimension. The $\partial/\partial y$ derivatives vanish and the natural boundary conditions are eliminated, which means $w_0 = w_0(x)$. The governing equation and boundary conditions are simply:

$$\frac{\mathrm{d}^4 w_0}{\mathrm{d}x^4} = \frac{q}{D^*} \quad , \quad D^* \equiv \frac{E_1 h^3}{12(1-\nu_{12}\nu_{21})} \tag{6a}$$

$$\Gamma_u : w_0 = 0 \quad , \quad \frac{\mathrm{d}w_0}{\mathrm{d}x} = 0 \quad , \quad x = \{0, l_B\} \tag{6b}$$

One should note the similarity between equation 6a and the classical beam bending equation. The difference is only in the bending stiffness under cylindrical bending which includes the Poisson's ratios due to the plane strain assumption. Figure 7 also shows the area where the cylindrical bending approximation is valid in red. For the SCBs investigated within the LDAinOp program the SCB span to length ratio is often larger than seven. Even for lower aspect ratio SCBs located in the inner region of the main wing ($s_{\text{sp}}/l_b > 2$) the approximation is reasonable for approximately 80% of the SCB span. In the outer region near the spoiler tips there is a complex spanwise deformation.

3.3. Structural Module

A structural module was developed based on the analytic element method (AEM) approach as described by Policarpo et al. [9]. This allows for a structural solver which is both accurate and efficient.

The module is then used in an optimization environment where the desired bump shapes are fed to the optimization algorithm through an objective function as target shapes in order to find the optimized design parameters that minimize the difference between the target shape (*i.e.* the desired aerodynamic bump shape) and the optimized shape.

Figure 8 shows the active surface of the SCB idealized as a series of plate strips spanning along the y direction which are actuated by the pressurized chambers inside the spoiler body. A spring is used to model the stiffness of the interface between consecutive chambers whose pressure is kept uniform.

Since the pressure inside each chamber is assumed to be uniform, the deflection of a point in the midplane of the strip plate actuated by the i^{th} chamber is

$$w_{0_i}(x) = \frac{p_i}{24 D_i^*}x^4 + C_1^i x^3 + C_2^i x^2 + C_3^i x + C_4^i \tag{7}$$

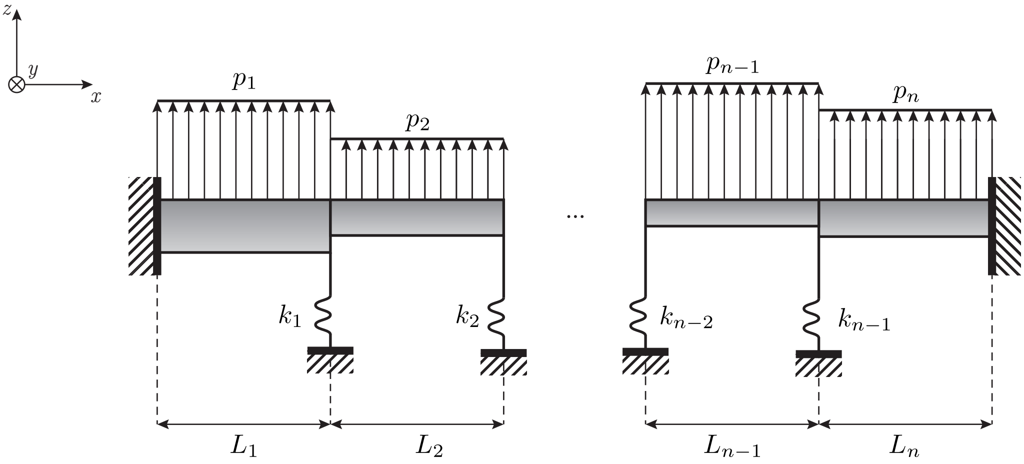

Figure 8 – Simplified 2D model used in the structural module

where D_i^* is the flexural rigidity of the i^{th} plate strip and C^i are the set of constants to be determined using the boundary conditions. The loads on the left (I), and right (J) nodes of each strip are given in terms of shear force (V) and bending moment (M) by

$$\left\{F^I \quad M^I \quad F^J \quad M^J\right\}_i^T = \left\{-V(x_i=0) \quad -M(x_i=0) \quad V(x_i=L_i) \quad M(x_i=L_i)\right\}_i^T \tag{8}$$

where x_i indicates a local reference framed centred on the I node. Similarly, it is possible to write the nodal degrees of freedom (DoF) (*i.e.* the nodal deflections and rotations) as a function of the C^i analytic constants. Noting that $\theta(x) = \mathrm{d}w_0/\mathrm{d}x$,

$$\left\{w_0^I \quad \theta^I \quad w_0^J \quad \theta^J\right\}_i^T = \left\{w_0(x_i=0) \quad w_0'(x_i=0) \quad w_0(x_i=L_i) \quad w_0'(x_i=L_i)\right\}_i^T \tag{9}$$

Using the shear force and bending moment definitions and eq.7 it is possible to rewrite eq.8 and eq.9 as follows,

$$\{F\} = [B]\{c\} + \{q\} \tag{10}$$

$$\{p\} = [C]\{c\} + \{g\} \tag{11}$$

where $\{F\}$ is the vector of nodal forces, $\{p\}$ is the vector of nodal DoF and $\{c\}$ is the vector containing the C^i analytic constants. Matrices $[B]$ and $[C]$ as well as vectors $\{q\}$ and $\{g\}$ are only functions of the plate strip parameters. Solving equations 10 and 11 simultaneously holds a familiar FEM representation

$$[K]\{p\} = \{F\} + \{f\} \tag{12}$$

where $[K]$ is the stiffness matrix and $\{f\}$ are the distributed loads. The relation with the original matrices is given by

$$[K] = [B][C]^{-1}\{p\} \tag{13}$$

$$\{f\} = \left([B][C]^{-1} - [I]\right)\{g\} \tag{14}$$

where $[I]$ is the 4×4 identity matrix. Therefore, the solver implementation is very similar to the FEM approach for both assembly and solving algorithms. The AEM maximizes accuracy because it retrieves the exact solution, while the FEM using typical Hermitian shape functions would retrieve the exact nodal displacements but underestimate the deflection between the nodes for a given distributed loading, leading to an underestimation of the required chamber pressure. The AEM also maximizes speed because it minimizes the number of elements required to describe each pressurized chamber which also contributes to the efficiency of the optimization algorithm.

3.4. Optimization Module

The optimization module uses the Nelder-Mead simplex direct search method [10] and includes variable transformation to address bound constraints for the optimization parameters. This can be used to define both design criteria constraints (*e.g.*: minimum active layer thickness and chamber length) as well as constraints imposed by pressure limits inside each chamber. The design parameters include:

- α_i - the relative position of each chamber interface as a percentage of the total spoiler chord. This is then used to compute the length L_i of each chamber;
- h_i - the thickness of the upper skin (active layer) of each chamber;
- k_i - the spring constant modelling the chamber walls stiffness;
- p_i - the actuation pressure of each chamber.

Any combination of design parameters might be fixed by the user, while the remaining variables are subject to the optimization process. It is also possible to choose the number of pressurized chambers which is directly related to the overall design complexity.

The initial set-up requires the user to input a base shape for the "clean" configuration, a target shape and the number of pressurized chambers. A set of bound constraints for the optimization parameters may be provided as well.

Fig.9 shows how the structural and optimization modules are integrated into the design tool algorithm.

The base and target shapes are first loaded and the user inputs the number of pressurized chambers. Each chamber is associated with a series of new optimization parameters. Adding chambers has therefore a very significant impact on the problem complexity. Moreover, increasing the number of optimization parameters has a disproportional effect on the number of calculations the optimization algorithm must perform and consequently leads to a rapid growth of the algorithm runtime.

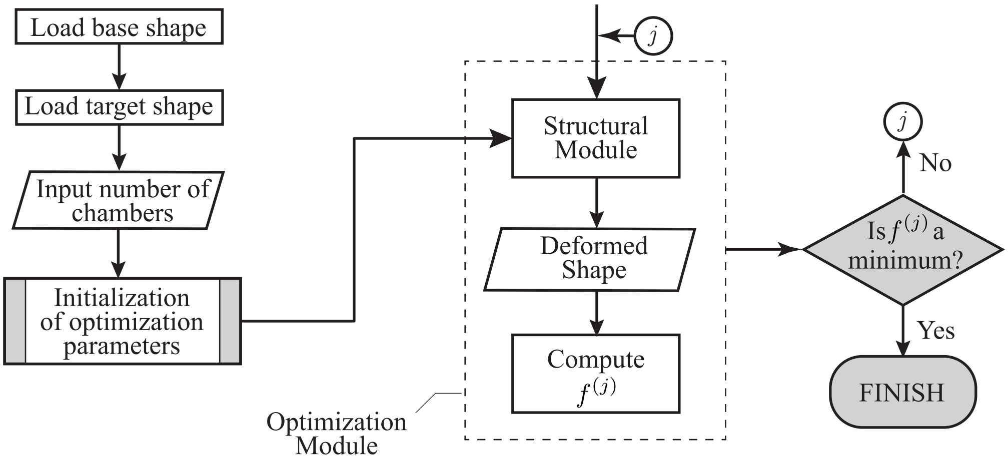

Figure 9 – Flow diagram for the design tool algorithm

The value $f^{(j)}$ refers to the objective function value at the end of the j^{th} iteration. The objective function evaluates the closeness, or in the strict sense of the optimization problem the lack-thereof, of the current iteration SCB shape to the target shape.

3.5. Objective Function

There are multiple ways of describing the conformity status of the current iteration shape to the target shape. The sensitivity of each possible implementation of the objective function to the optimization parameters will have a profound effect on the algorithm efficiency and accuracy. Moreover, since the simplex method does not ultimately converge to a minimizer for general (nonconvex) functions, a poor choice of objective function might even prevent reaching a solution. Finally, the greater the size of the optimization problem, the more difficult it is to obtain good solutions. For this reason, the performance of different objective functions has been evaluated. For consistency in the evaluation, only actual solutions of equation 6a have been used as target shapes during the validation process.

3.5.1. *Maximum Distance*

A simple way to evaluate the conformity is to use an objective function that retrieves the maximum distance between the two curves describing the current and target bump shapes. Assuming a piecewise linear approximation of the target shape, the distance between a point $C_m = (x_0, y_0)$ on the current shape to two consecutive points $T_n = (x_n, y_n)$ and $T_{n+1} = (x_{n+1}, y_{n+1})$ on the piecewise linear approximation of the target shape is

$$\left\|C_m \to T_n, T_{n+1}\right\| = \frac{|(y_{n+1}-y_n)x_0 - (x_{n+1}-x_n)y_0 + x_{n+1}y_n + y_{n+1}x_n|}{\sqrt{(y_{n+1}-y_n)^2 + (x_{n+1}-x_n)^2}} \tag{15}$$

If a line passing trough C_m and normal to the direction formed by points T_n and T_{n+1} intersects the segment $\overline{T_n T_{n+1}}$, then equation 15 computes the minimum distance of point C_m to the piecewise linear approximation of the target shape. Repeating this process for a set of M points along the current shape, one obtains a set of distances from points on the current shape to a map of those points on the target shape. The optimization problem is now minimizing the maximum distance in that set. The objective function is:

$$f_1 = \max_{C_m \in \Gamma_C} \left(\left\| C_m \rightarrow T_n, T_{n+1} \right\| \right) \quad , \quad n = 1, 2, \ldots, N \quad , \quad m = 1, 2, \ldots, M \tag{16}$$

Figure 10 shows how point C_m can be mapped to line segment $\overline{T_n T_{n+1}}$ but cannot be mapped to segments $\overline{T_{n-1} T_n}$ and $\overline{T_{n+1} T_{n+2}}$: the intersection point of the normal to those segments containing C_m lies on an extension an not on on the actual segments. Using the same reasoning, point C_{m+1} must be mapped to the segment $\overline{T_{n+1} T_{n+2}}$.

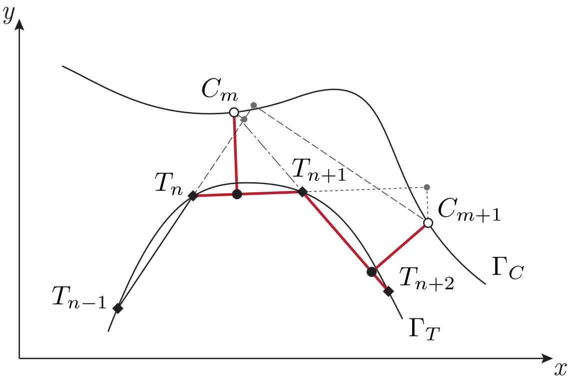

Figure 10 – Distance from points on the candidate shape Γ_C to the target shape Γ_T

3.5.2. *Area Difference*

Another approach to evaluate conformity is to evaluate the area enclosed between the current and the target shapes. The optimization problem is now the minimization of that area. The objective function is:

$$f_2 = \int_0^{l_b} \left| f_C^{(i)}(x) - f_B(x) \right| \mathrm{d}x \tag{17}$$

where $f_C^{(j)}$ is the shape function of the candidate shape at the end of the j^{th} iteration and f_B is the shape function of the target shape. Unlike the previous implementation, the conformity status at each iteration now contains information from the entire domain of the current shape versus only one point that might change location arbitrarily from one iteration to the next. Therefore, it is expected that f_2 might stabilize and accelerate the optimization process.

3.5.3. *Weighted Area Difference*

A variation on the last objective function can be made through a weight function $\phi(x)$. As mentioned, the correct position of the SCB crest has the strongest influence on the drag reduction potential. Unfortunately, the previous implementations were not capable of enforcing special priority to geometrical conformity around the crest position. Using a weight function $\phi(x)$ that introduces a penalty by amplifying the area difference around the crest position, that is now possible.

$$f_3 = I(\phi) = \int_0^{l_b} \phi(x) \left| f_C^{(j)}(x) - f_B(x) \right| \mathrm{d}x \tag{18}$$

This might accelerate the optimization process when the target shape is a physical solution of equation 6a. However, it is most useful if the desired target shape is not a physical solution. In this case, the best physical approximation to the target shape might lead to a large offset of the crest position. Using a weighting function, the general conformity might be relaxed in exchange for better crest conformity.

3.6. Target Shapes

The design tool allows the optimization process for any parametrization of the target shape. However, this study is focused on the structural realization of the SCB and therefore common parametrizations used in aerodynamic investigations might be inefficient from an actuation point of view. Nevertheless, since the crest position is the main geometrical factor affecting SCB performance, there is freedom to generate target shapes more easily actuated while still achieving comparable efficiency gains.

As from the time of submitting this study, an algorithm that generates actuation-optimized physical solutions containing a prescribed crest position is under development. However, a simple yet non-optimal solution has already been implemented.

A common problem with typical parametrizations used in aerodynamic studies is the different slopes that the ramp and tail sections of the SCB show when the crest position is closer to the leading or trailing edge. Figure 11 shows the typical "overshoot" that happens on the final optimized shape when the target shapes are generated using a cubic spline containing only the peak position P and both leading (O) and trailing (l_B) edges. The target shape is very asymmetric around the peak position and the asymmetry increases as the peak moves towards the edges.

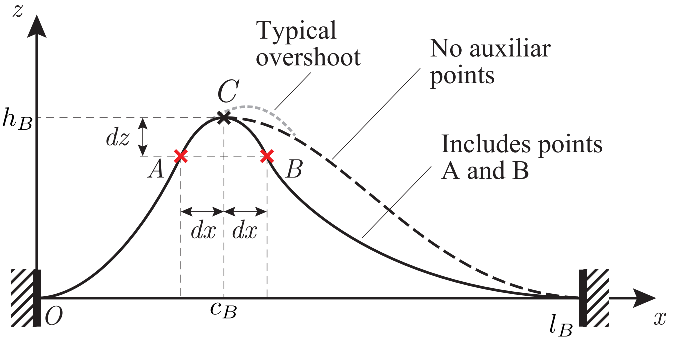

Figure 11 – Generation of target shapes

Enforcing some degree of local symmetry around the crest using auxiliary points $A = (c_B - dx, h_B - dz)$ and $B = (c_B + dx, h_B - dz)$ helps mitigate the overshoot. Values of dx and dy that better approximate the actual physical behaviour of the SCB will then have to be determined. When interpolating point B, the slope is averaged using

$$\left.\frac{dz}{dx}\right|_B = \frac{c_B\left(-\left.\frac{dz}{dx}\right|_A\right) + \left(\frac{l_B}{2} - c_B\right) m_{\overline{Bl_B}}}{\frac{l_B}{2}} \tag{19}$$

so that when $c_B = l_B/2$ the curve is perfectly symmetric (*i.e.* $dz/dx|_A = -dz/dx|_B$). The case $c_B = 0$ corresponds to the limit when B would be exactly vertical to O and $dz/dx|_B = m_{\overline{Bl_B}}$, where $m_{\overline{Bl_B}}$ is the slope of the straight line connecting point B to the trailing edge. For crest positions closer to the trailing edge, the process is followed by a reflection around $x = l_B/2$.

4. RESULTS

4.1. Comparison of Objective Functions

In general, all objective functions presented are able to conform the SCB to the typical class of shape functions used in most aerodynamic studies (*e.g.* polynomials, beam functions or even parametrizations using Hicks-Henne shape functions), provided a good initial estimation of the optimization parameters. However, their convergence rate is different and the final result might be strongly affected by the quality of the initial estimation, ultimately leading to different results. To illustrate this, an extreme example is presented using a target shape generated from the physical solution for a 2-chamber SCB made of 1 mm thick UD fibreglass plate strips subject to $p_1 = 3 \times 10^3$ Pa and $p_2 = -1.75 \times 10^3$ Pa with a chamber interface located at $40\% l_B$, *i.e.* $\alpha_1 = 0.4$. A poor initial guess for the optimization parameters was purposefully chosen: $p_1 = -1 \times 10^3$ Pa, $p_2 = 1 \times 10^3$ and $\alpha_1 = 0.3$. Additionally, $\alpha_1 \in [0.25, 0.75]$.

Figure 12(a) shows the initial approximation obtained using a poor estimation of the optimization parameters which deviates significantly from the target shape. Figure 12(b) shows the results of the optimization process using objective functions f_1 and f_2. For the sake of simplicity, details regarding objective function f_3 using the weighted area difference will be left out of this study as they would require an extensive analysis due to many alternatives for the choice of weight functions and their effect on different types of shape parametrization. However, it is clear that using f_1 results in a poor optimized shape. This is due to the poor estimation of the optimization parameters combined with the tendency for arbitrary change in location of the point of maximum distance during the initial

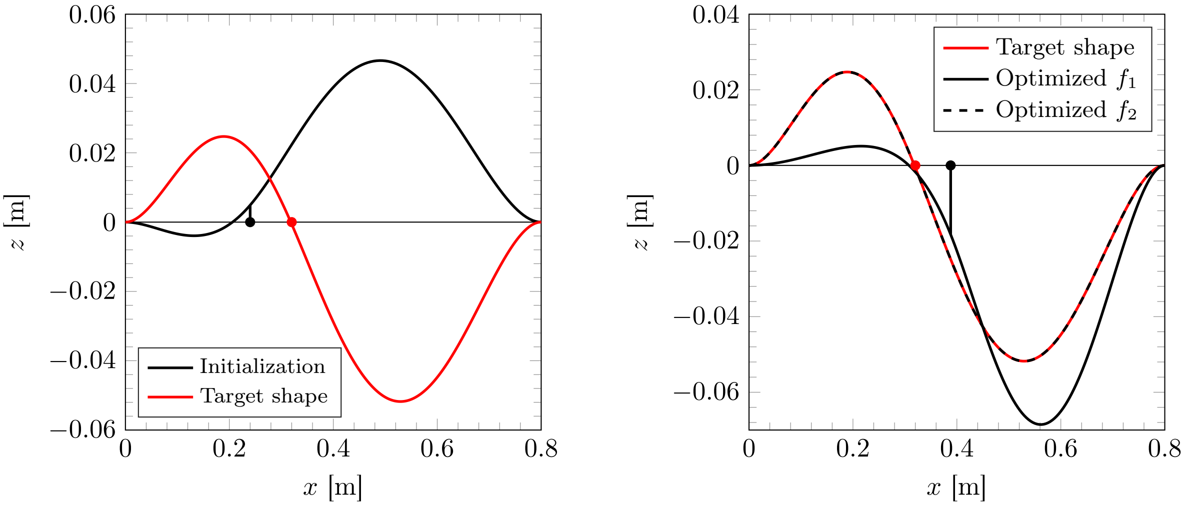

(a) Initialization results.

(b) Final optimization results.

Figure 12 – SCB shapes for the initialization and optimization - the chamber interface is represented by the circular marker.

stages of the optimization process that ultimately introduces too much noise in the Nelder-Mead algorithm, thus preventing convergence to a global minimizer. As expected, f_2 does indeed stabilize the optimization process and is therefore able to achieve the target physical solution even with a poor initialization.

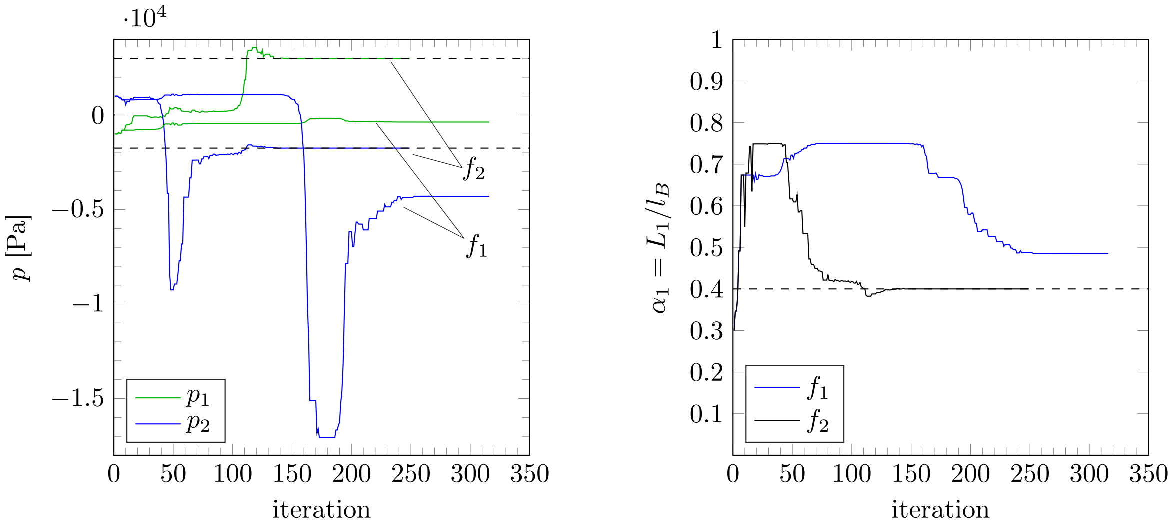

(a) Actuation pressure

(b) Chamber length

Figure 13 – Evolution of the optimization parameters

Figure 13 shows the evolution of the optimization parameters. The horizontal dashed lines represent the actual values of actuation pressure and chamber length used to generate the target shape. Using f_2 not only retrieves the exact values used for validation (unlike f_1), but the optimization process converges 1.7 times faster.

4.2. Target Shapes

Figure 14 illustrates the impact that the target shape has on the optimized crest position of a two chamber spoiler design. Different target shapes that include the same crest position $C(c_B = 0.35l_B,\, h_B = 0.05l_B)$ are compared. The curves have been vertically spaced for visualization purposes only.

Target shape A uses no auxiliary points and the peak “overshoot” is the highest in both x and y directions. The other curves include auxiliary points with fixed $dy = 0.10h_B$ and varying values of dx. Target B and C represent two extreme cases. Curve B has a large value of dx and the target crest radius is too large. The crest of the optimized shape has too much vertical displacement. Curve C has a small dx which means the target crest radius is too small and the optimized shape has too little vertical displacement. However, it is clear that adding auxiliary points greatly improves the chordwise positioning of the crest in both cases due to the local symmetry enforcement.

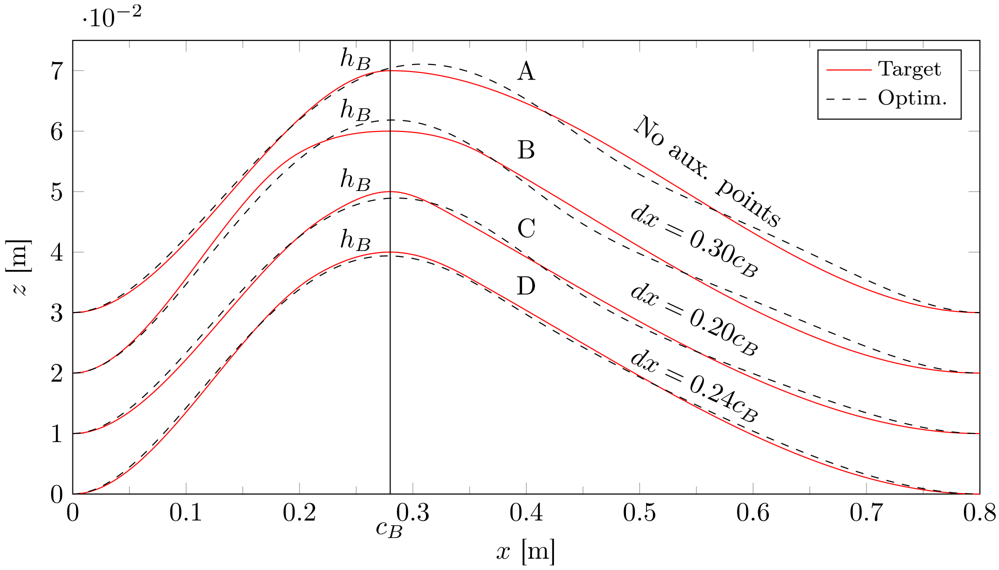

Figure 14 – Effect of parameters dx and dy

Curve D shows that after proper adjustment of the values dx and dy it is possible to generate non-physical target shapes that are also more easily actuated using the correction mechanism proposed.

4.3. Deformation Envelope

Since the optimal bump shape varies according to different flight conditions, there is the need for an envelope of bump deformations. In this section, a simple flat spoiler is considered and a set of bump shapes are generated by varying the longitudinal crest position.

Figure 15(a) shows the deformation envelope for a group of peak positions ranging from 20% to 45%l_B while h_B is kept constant $h_B = 5\%l_B$. The dashed vertical lines represent the optimal position of the two chamber interface for each target shape.

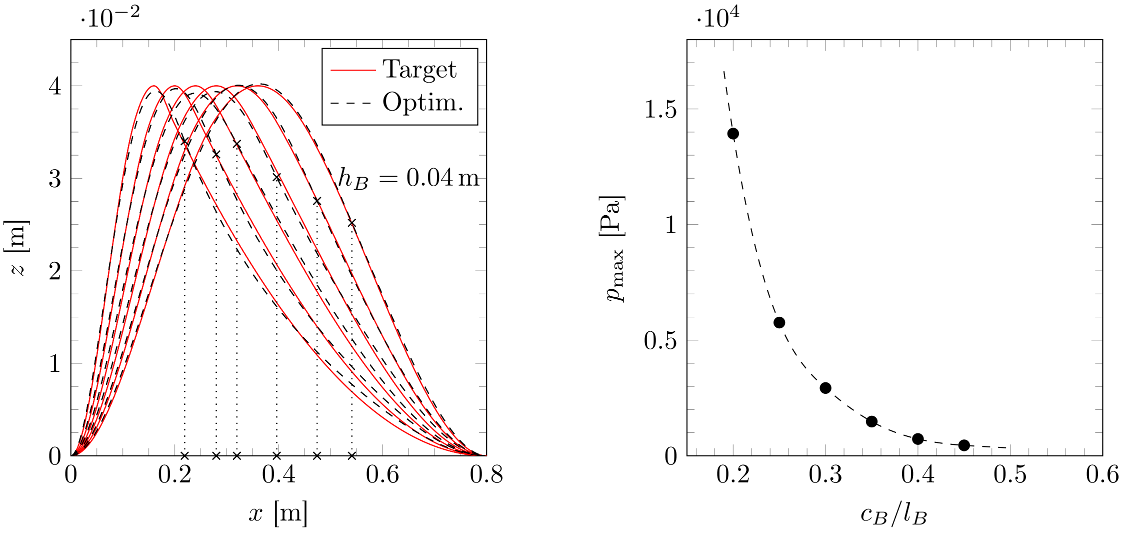

(a) Typical deformation envelope.

(b) Typical actuation envelope.

Figure 15 – Deformation and actuation envelopes for a two chamber SCB.

The deformation envelope can be completed with an actuation envelope, computed by plotting the maximum chamber pressure against the crest position. Figure 15(b) shows the actuation envelope that results from the deformation envelope presented in fig.15(a) for the two chamber design.

For the two chamber SCB, the minimum actuation pressure happens when the crest position is located in the middle of the plate. As the crest moves towards the edges, the pressure starts increasing disproportionately as a consequence of the greater deformation level required for such configurations. The actuation envelope is therefore symmetric to $c_B/l_B = 0.5$.

The actuation pressure can vary considerably as the optimal crest position changes due to aerodynamic reasons, drawing attention to the fact that, once a chamber configuration is chosen, generating bumps in off-design conditions can become extremely inefficient. This means that a detailed aerodynamic study must be carried out for each specific aircraft in order to ensure that the required deformation envelope (determined by the aerodynamics) is located in the most favourable region of the actuation envelope (to increase actuation efficiency).

4.4. Number of Chambers

The number of pressurized chambers directly affects the weight and complexity of the spoiler structure. Therefore, the influence of the number of chambers on the actuation efficiency was investigated. The same spoiler is used to generate a deformation envelope identical to the one in fig.15(a) using now three chambers.

Figure 16(a) shows the new actuation envelope: the maximum actuation pressure is no longer symmetric due to the stiffness of an additional chamber interface. Again, as the crest position moves towards the edges, the required maximum pressure increases significantly as expected.

To better assess the effect of an additional chamber, figure 16(b) shows the relative difference between maximum chamber pressures for the two configurations in study.

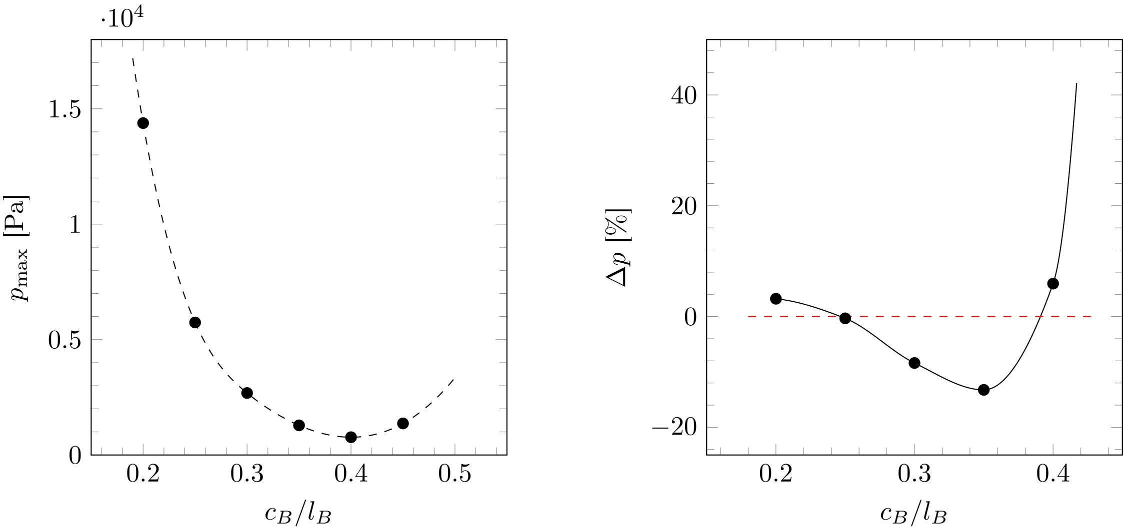

(a) Actuation envelope for the three chamber SCB.

(b) Maximum actuation pressure difference between three and two chamber SCBs.

Figure 16 – Evaluation and comparison of a three chamber SCB.

Even though there is a loss of structural efficiency for the outermost regions of the spoiler, the inner region actually benefits from a lowering of up to 13% of the maximum actuation pressure compared to the two chamber configuration. As the number of chambers increases, the region where the maximum actuation pressure is lower than less complex designs becomes narrower.

4.5. Spoiler Tips

The design of the spoiler tips has a great impact on the actuation performance of the SCB and its capacity not only to conform to the desired crest position, but also to maintain an aerodynamically acceptable shape. In this section, three different designs for the spoiler tips are considered: a spoiler with open ends (and thus free tips); a spoiler with fixed tips and a spoiler whose ends have been closed using the same material of the upper spoiler skin.

The results are computed using a commercial FEM code and a complete 3D spoiler model. Fig.17(a) shows the deformation for each design: the dashed curves represent the deformation of the spoiler tips (*i.e.* upper skin edge at both spoiler ends) and the solid lines show the deformation in the half span of the spoiler.

For the spoiler configuration with free tips, the bump profiles on the spoiler tips and half span present little variation. Moreover, the half span bump is exactly coincident with the bump shape predicted by the structural solver that was developed. However, the full 3D model shows that the outermost region of the spoiler experiences some additional spanwise deformation as expected.

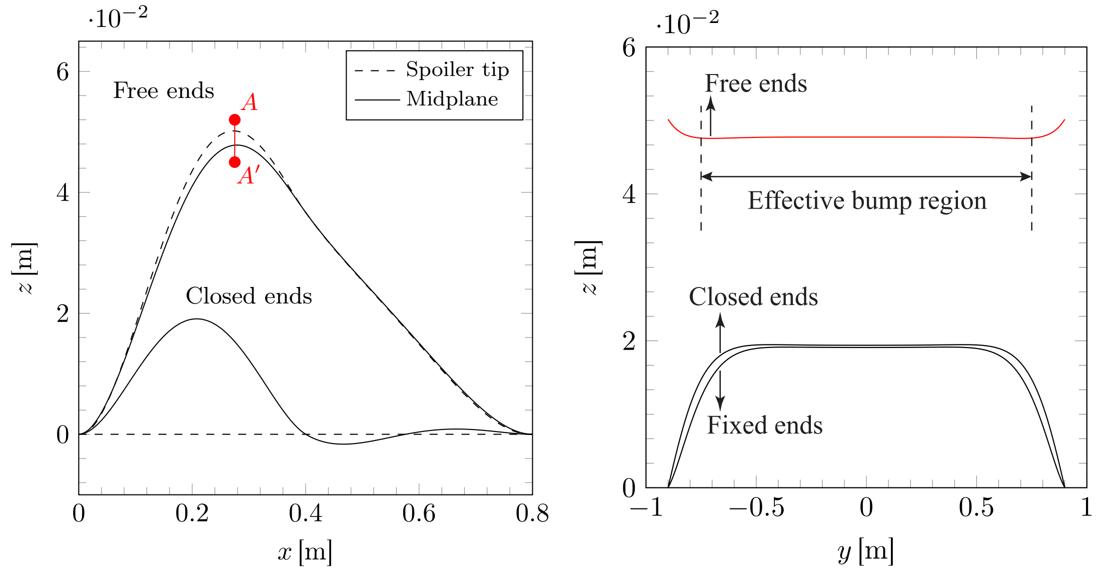

(a) SCB profiles along the span for different closing configurations.

(b) Span-wise crest deformation.

Figure 17 – Profile and spanwise deformation for different spoiler configurations.

The designs with closed and fixed ends are much stiffer. Both designs present identical deformations and for that reason only the closed end variant is depicted in fig.17(a). The additional stiffness introduced by the closing plates has a dramatic effect on the deformation of the spoiler tip which now behaves as if it were fixed. The inner region is also greatly affected: not only is the deformation much lower than desired, but the longitudinal crest position is considerably different. The bump profile is also completely altered and a “wavy” region near the spoiler trailing edge appears.

Figure 17(b) presents the span-wise evolution of the crest deflection obtained by inspecting the upper skin deformation along a plane AA' coincident with the peak position as shown in figure 17(a). The same was done along the fixed and closed end designs. The latter have almost the same spanwise deformation except for a region near the tips where the spoiler with the closing plates presents a slightly larger deformation. In any case, such configurations lead to completely different solutions, showing that the structural model developed can only be used for accurate predictions if the spoiler has free ends. Again, the red line in figure 17(b) shows that there is indeed a considerably large region (“the effective bump region”) where the current model provides accurate predictions and can be used as a useful design tool.

5. CONCLUDING REMARKS

A structural concept using pressurized chambers is presented for the structural realization of an adaptive SCB. Using a simplified 2D parametric model, the influence of selected design parameters was investigated. The effect of an increasing number of chambers on the actuation pressure and chamber design was also studied. The deployment of the bump for various designs of the spoiler ends was presented. Since the crest position is the driving aerodynamic parameter, a method for generating easily actuated bump shapes was proposed.

The concept suggested has enough freedom to conform to a wide range of bump shapes even for a two chamber design. It has been shown that increasing the number of chambers can lead to a reduction of the actuation pressure, but since each chamber interface contributes to added flexural rigidity of the active layer, this effect can only be used within a limited region of crest positions and up to a maximum number of chambers.

The design of the spoiler ends has been shown to have both a strong impact on the ability of the structure to conform to the desired crest position and also on the quality of the entire target shape.

ACKNOWLEDGEMENTS

The work was funded by the 5th Federal Aeronautical Research Program (LUFO V) by the Federal Ministry of Economic Affairs and Energy (BMWi) in the project LDAinOP, FkZ: 20A1302B.

REFERENCES

[1] Smith, J.W., Lock, W.P., Payne, G.a., “Variable-camber systems integration and operational performance of the AFTI/F-111 mission adaptive wing”, Proceedings of NASA Technical Memorandum 4370, 1992.

[2] Stanewsky, E., Délery, J., Fulker, J., Geißler, W. (Eds.), EUROSHOCK - Drag Reduction by Passive Shock Control: Results of the Project EUROSHOCK, AER2-CT92-0049 Supported by the European Union, 1993 - 1995 (Notes on Numerical Fluid Mechanics) (Volume 56), Vieweg+Teubner Verlag, Braunschweig, Germany, 1 ed., 1997.

[3] Stanewsky, E., Délery, J., Fulker, J., de Matteis, P., Drag Reduction by Shock and Boundary Layer Control: Results of the Project EUROSHOCK II. Supported by the European Union 1996-1999, vol. 80, Springer - Verlag Berlin Heidelberg GmbH, 1 ed., 2002.

[4] Ashill, P., Lock, W.W., “A novel technique for controlling shock strength of laminar flow aerofoil sections”, Proceedings of Proceedings 1st European Forum on Laminar Flow Technology March 16-18th, 1992, DGLR, AAAF, RAeS, Hamburg, Germany, acta astro ed., 1992, pp. 175–183.

[5] Dargel, G.D.B.A.A.G., Rodde, A.O., Archambaud, J.P.O.C., “Assessment of the Capability of Drag Reduction of the Shock Control Device "SC Bump" on Airfoil Flows and Application Aspects on Wings”, Proceedings of IUTAM Symposium on Mechanics of Passive and Active Flow Control, vol. 53, Springer Netherlands, 1999, pp. 57–62.

[6] Sommerer, A., Lutz, T., Wagner, S., “Numerical Optimization of Adaptive Transonic Airfoils with Variable Camber”, Proceedings of Proceedings 22nd ICAS Congress, Harrogate, UK, Harrogate, United Kingdom, 2000, pp. 2111.1–2111.10.

[7] Wadehn, W., Sommerer, A., Lutz, T., Fokin, D., Pritschow, G., Wagner, S., “Structural Concepts and Aerodynamic Design of Shock Control Bumps”, Proceedings of ICAS Congress - Congress of International Council of the Aeronautical Sciences, Toronto, 2002, pp. 66R1.1–66R1.10.

[8] Bein, T., Hanselka, H., Breitbach, E., “An adaptive spoiler to control the transonic shock”, Smart Materials and Structures, 9(2), 2000, pp. 141–148.

[9] Policarpo, H., Matos Neves, M., “Using symbolic computation for teaching structural mechanics I: frames”, Proceedings of CSEI2012 – Conferência Nacional sobre Computação Simboólica no Ensino e na Investigação, Lisbon, Portugal, 2012, pp. 1–13.

[10] Lagarias, J.C., Reeds, J.A., Wright, M.H., Wright, P.E., “Convergence Properties of the Nelder–Mead Simplex Method in Low Dimensions”, SIAM Journal on Optimization, 9(1), 1998, pp. 112–147.

[11] Kintscher, M., Wiedemann, M., “Design of a Smart Leading Edge Device”, Proceedings of M. Wiedemann, M. Sinapius (Eds.), Adaptive, tolerant and efficient composite structures, chap. 31, Springer - Verlag Berlin Heidelberg GmbH, 1 ed., 2012, pp. 381–390.